




Transient retrograde motion of spin wave driven skyrmions in magnetic nanotracksLin Huang , Gavin Burnell , and Christopher H. Marrows ^{*}*School of Physics and Astronomy, University of Leeds, Leeds LS2 9JT, United Kingdom*

(Received 30 January 2023; revised 26 May 2023; accepted 31 May 2023; published 20 June 2023)

The motion of a skyrmion driven by propagating spin waves in a thin film track with interfacial perpendicular magnetic anisotropy and Dzyaloshinskii-Moriya interaction was investigated by numerical micromagnetic simulations. At long simulation times, we find that the skyrmion always moves in the direction of the spin-wave propagation. At shorter times, rather than observing skyrmion motion in a single direction, the skyrmion shows transient retrograde motion when the track width is wider than 50 nm (for Gilbert damping $\alpha = 0.02$) or $\alpha < 0.06$ (for a track width of 100 nm). A simple treatment of spin-wave-driven skyrmion motion based on the Thiele equation predicts that the skyrmion will be pulled back towards the source of the spin waves because of the gyrotropic and dissipative effects. The forward motion away from the spin wave source can be explained by also considering the effect of a repulsive force from the edges of the track when the skyrmion is in close contact with it. We discuss these effects quantitatively in terms of the spin-wave transmission and reflection coefficients of the skyrmion.

DOI: [10.1103/PhysRevB.107.224418](https://doi.org/10.1103/PhysRevB.107.224418)**I. INTRODUCTION**

A magnetic skyrmion can be regarded as a topologically protected spin texture [1], stabilized by the Dzyaloshinskii-Moriya interaction (DMI) [2]. In multilayers of ferromagnetic (FM) and heavy metals, the DMI can arise at interfaces with a strength that is adjustable by changing the thickness or type of components, offering the ability to tune the size and stability of Néel skyrmions that are stable at room temperature [3]. These skyrmions' small size and stability make them magnetic elements that are of high interest for device applications in multilayer thin films [4]. For instance, the high-speed dynamics caused by low-energy excitation [5–8] makes skyrmions a potential magnetic element to store and carry data in spintronic devices. Many researchers have high expectations of the performance of skyrmions to either replace some conventional microelectronic devices or introduce new functionality [9,10].

Spin torques arising from electrical currents are a means to drive skyrmion motion that has been widely studied [5–8], but the Joule heating produced by these currents can affect the spintronic device performance. Meanwhile, the reduced heating [11,12] and concomitant reduced energy consumption [13] from skyrmion motion driven by spin waves (SWs) means that this topic has attracted increasing attention.

For instance, a SW with twisted orbital angular momentum can give rise to a skyrmion with a rotated gyration motion [14]. A skyrmion crystal in Cu_2OSeO_3 can be rotated by the Magnus force from both SW and thermal gradient [15,16]. Under a transverse field to the skyrmion, the differently propagating SWs will also give rise to a skyrmion diode effect for a certain SW frequency and sample width [17]. Simulations of SW-controlled skyrmion motion in materials with different Gilbert damping coefficients [11] or frequencies of SWs [18] show the controllability of skyrmion speed and displacement by this means. The motion of skyrmions at corners and T junctions shows skyrmions preferring to turn in different directions depending on the SW propagation direction [11]. The form of the skyrmion can also be used to control the direction of re-emitted SWs [19]. The forces arising from spin-transfer torque (STT) and linear momentum transfer between SW magnons and skyrmions give rise to different directions of skyrmion motion, towards and away from the SW source, respectively [17,20,21]. The retrograde motion of a Bloch domain wall because of the decreasing effect from a transmitted SW was also studied by Wang *et al.* [22,23]. Here we study the specific circumstances of a Néel-type skyrmion instead of a Bloch domain wall in which these different behaviors can be found. The predicted skyrmion motion can inform the design of spintronic or magnonic logic gates and other functional devices.

Numerical micromagnetic simulations are well-suited to studying SW-driven skyrmion dynamics, and there are many recent examples, in most of which the track for the skyrmions is narrower than 100 nm or not larger than four times the skyrmion diameter [11,17,18,20,21,24]. By studying the skyrmion motion in tracks of different width, we can predict the skyrmion motion in an experimentally achievable sample. We also study the SW-driven skyrmion motion as a function of varying the Gilbert damping constant. Our

^{*}c.h.marrows@leeds.ac.uk

simulations were carried out with the micromagnetics package OOMMF [25]. The simulation is based on iteration of the Landau–Lifshitz–Gilbert equation:

$$\frac{d\mathbf{M}}{dt} = -\gamma\mathbf{M} \times \mathbf{H}_{\text{eff}} + \frac{\alpha\mathbf{M}}{M_s} \times \left(\frac{d\mathbf{M}}{dt}\right), \quad (1)$$

which is an equation of motion for the magnetization \mathbf{M} , where $\gamma = -2.211 \times 10^5 \text{ mA}^{-1}\text{s}^{-1}$ and α are the gyromagnetic ratio and Gilbert damping constant, respectively. (Here and throughout, we use SI units unless otherwise specified.) M_s is the saturation magnetization. \mathbf{H}_{eff} describes the effective fields in the system arising from energy terms such as the exchange stiffness, DMI, and anisotropies as well as the applied magnetic field [11], defined as the partial derivative of the free energy density E with respect to the magnetization \mathbf{M} ,

$$\mathbf{H}_{\text{eff}} = -\frac{1}{\mu_0} \frac{\partial E}{\partial \mathbf{M}}, \quad (2)$$

in which $\mu_0 = 4\pi \times 10^{-7} \text{ H/m}$ is the vacuum permeability. The free-energy density contains terms arising from the magnetic field \mathbf{H} , which includes both the external applied field and the demagnetization field, Heisenberg exchange with exchange stiffness A_{ex} , uniaxial anisotropy with anisotropy constant K_u and easy axis direction with unit vector $\hat{\mathbf{u}}$, and interfacial DMI [25], and is written as

$$E = -\mu_0\mathbf{M} \cdot \mathbf{H} + A_{\text{ex}}\nabla \cdot \left(\frac{\mathbf{M}}{M_s}\right)^2 - K_u \left(\frac{\mathbf{M}}{M_s} \cdot \hat{\mathbf{u}}\right)^2 + E_{\text{DMI}}, \quad (3)$$

where the interfacial DMI energy is written as [26]

$$E_{\text{DMI}} = \frac{D_{\text{DMI}}}{M_s^2} \left(M_z \frac{\partial M_x}{\partial x} - M_x \frac{\partial M_z}{\partial x} + M_z \frac{\partial M_y}{\partial y} - M_y \frac{\partial M_z}{\partial y} \right), \quad (4)$$

with interaction strength D_{DMI} .

Here we report micromagnetic simulations of SW-driven skyrmion motion and find two behaviors: Either the skyrmion starts to move away from the SW source immediately and continues to do so or else undergoes a transient retrograde motion where it initially moves towards the SW source before changing direction to give a similar long-term motion away from the source. The transient retrograde motion occurs in tracks wider than 50 nm when $\alpha < 0.06$. We identify the long-term motion away from the SW source, contrary to the expectations from Ref. [21] and similar to Ref. [27], as a gyrotropic effect arising from an additional force on the skyrmion arising from its repulsive interaction with the edge of the track.

We also determined the SW transmission and reflection coefficients of the skyrmion from the results of our micromagnetic simulations of skyrmion motion and use these to inform analytical models of the skyrmion dynamics based on the Thiele equation [28,29]. We show that this approach can give a good quantitative account of the skyrmion motion during the initial part of the retrograde motion and the long-term forward motion along the track edge, but other effects must be at play around the turning point of the motion.

II. SKYRMION DYNAMICS IN RESPONSE TO DRIVING FORCES

In this section, we briefly review some relevant results on skyrmion motion to introduce some concepts that we shall use later to describe our work.

The Thiele equation describes the dynamics of rigid magnetization textures in response to driving forces [28], and was originally derived to treat bubble domains. It can thus also be used to treat the motion of skyrmions in response to driving forces such as a current of magnons arising from a SW [29–31]. For a skyrmion spin texture with spatial coordinate \mathbf{R} , it is written as

$$\mathbf{G} \times \mathbf{v} - \alpha \mathcal{D} \cdot \mathbf{v} = -\mathbf{f}(\mathbf{R}), \quad (5)$$

where the gyrovector $\mathbf{G} = (0, 0, G) = (0, 0, -4\pi Q)$, for a skyrmion with topological charge $Q = -1$. $\mathbf{v} = \dot{\mathbf{R}}$ is the velocity of skyrmion, while \mathcal{D} is a dissipative tensor with the form $\begin{pmatrix} \mathbb{D} & 0 & 0 \\ 0 & \mathbb{D} & 0 \\ 0 & 0 & 0 \end{pmatrix}$ for an isolated skyrmion in a thin film [8].

$\mathbf{F} = -\nabla U$ is the force which is defined as the negative spatial derivative of the skyrmion potential energy U . Because of the \mathbf{H}_{eff} definition and $f_u = \gamma \int_S \mathbf{H}_{\text{eff}} \cdot \frac{d(\frac{\mathbf{M}}{M_s})}{d\mathbf{u}} dS$, where S is the nonuniform magnetization surface and \mathbf{u} can be either x or y , the converted force is represented in Eq. (5) by $\mathbf{f} = \mathbf{F}\gamma / (M_s \mu_0 d_M)$, where d_M is the thickness of the magnetic layer [32], since a quantity with dimensions of velocity is required in that form of the Thiele equation.

This yields

$$\begin{aligned} \mathbf{G} \times \mathbf{v} - \alpha \mathcal{D} \cdot \mathbf{v} &= (4\pi Q v_y - \mathbb{D} \alpha v_x, -4\pi Q v_x - \mathbb{D} \alpha v_y, 0) \\ &= (-f_x, -f_y, 0), \end{aligned} \quad (6)$$

from which we obtain

$$v_x = \frac{1}{G^2 + \alpha^2 \mathbb{D}^2} (4\pi Q f_y + \alpha \mathbb{D} f_x) \quad (7)$$

and

$$v_y = \frac{1}{G^2 + \alpha^2 \mathbb{D}^2} (-4\pi Q f_x + \alpha \mathbb{D} f_y). \quad (8)$$

Motion in the x direction is of particular interest here, since we define that as the SW propagation direction. The presence of the gyrotropic term in Eq. (5) means the y component of force will also affect the skyrmion velocity along the x axis, as shown in Eq. (7).

Here, we consider the driving force $\mathbf{f}(\mathbf{R})$ on the right-hand side of Eq. (5) as arising from two sources. The principal source is the SW magnon current drive, \mathbf{f}_{mag} , that can include the scattering of SWs as well as the reflection, transmission, and absorption of SWs. Nevertheless, the repulsion at the edge of the sample also plays a role. Thus, we write $\mathbf{f} = \mathbf{f}_{\text{mag}} + \mathbf{f}_{\text{edge}}$ [12].

Taking the edge force \mathbf{f}_{edge} first, following Ref. [12], we write the repulsive force from the edges of a nanostrip of width w across the y direction and thickness d_m as a function

of skyrmion position y :

$$\begin{aligned} \mathbf{F}_{\text{edge}} &= -V_{\text{edge}} \nabla \left[\exp\left(\frac{-(y + \frac{w}{2})}{L_{\text{edge}}}\right) + \exp\left(\frac{(y - \frac{w}{2})}{L_{\text{edge}}}\right) \right] \\ &= \mathbf{f}_0 \left[\exp\left(\frac{-(y + \frac{w}{2})}{L_{\text{edge}}}\right) + \exp\left(\frac{(y - \frac{w}{2})}{L_{\text{edge}}}\right) \right] \frac{M_s \mu_0 d_m}{\gamma}, \end{aligned} \quad (9)$$

where V_{edge} is used to parametrize the strength of the repulsion, and the penetration depth of the magnetization twist being induced by the DMI at the sample edges is L_{edge} . We define l_{edge} as the normalized length:

$$l_{\text{edge}} = L_{\text{edge}} / \sqrt{2A_{\text{ex}} / (\mu_0 M_s^2)}. \quad (10)$$

The physical parameters \mathbf{f}_0 and l_{edge} can be expressed in term of the dimensionless parameters $\Xi = D_{\text{DMI}} \sqrt{2 / (\mu_0 M_s^2 A_{\text{ex}})}$, $\kappa = 2K_u / (\mu_0 M_s^2)$, and $\eta = H_z / M_s$ [33]. Here, H_z is the external out-of-plane magnetic field. We can then write the values of the force and interaction depth as

$$|\mathbf{f}_0| = \frac{e\pi}{\sqrt{2}} \left(\Xi - \frac{2}{|l_{\text{edge}}|} \right) \sqrt{\frac{2A_{\text{ex}} \gamma^2}{\mu_0}}, \quad (11)$$

in which $e \approx 2.71828$ is Euler's number, and

$$|l_{\text{edge}}| = \frac{\pi^3 \Xi}{-4(\pi^2 - 4)\eta + 2\pi^2 \kappa}. \quad (12)$$

Then, considering the effect of SWs impinging on a skyrmion and scattering from it, in Ref. [12], the authors considered the force arising from SW scattering on the skyrmion, with a decay of the scattering force based on the SW attenuation owing to the distance between the SW source and skyrmion position \mathbf{R} . The scattering force is written as

$$\begin{aligned} \mathbf{f}_{\text{scatter}}(\mathbf{R}) &= j e^{-\frac{\mathbf{R} \cdot \hat{\mathbf{q}}}{L_{\text{mag}}}} q (\sigma_{\parallel} \hat{\mathbf{q}} + \sigma_{\perp} (\hat{\mathbf{z}} \times \hat{\mathbf{q}})) \\ &= j e^{-\frac{\mathbf{R} \cdot \hat{\mathbf{x}}}{L_{\text{mag}}}} q (\sigma_{\parallel} \hat{\mathbf{x}} + \sigma_{\perp} \hat{\mathbf{y}}) \end{aligned} \quad (13)$$

$$= f_{\text{scatter} \parallel} \hat{\mathbf{x}} + f_{\text{scatter} \perp} \hat{\mathbf{y}}, \quad (14)$$

where $\mathbf{q} = \hat{\mathbf{q}}q$ is the wave vector of the SW, assumed to be along the x direction, and j is the magnon current density $j = \frac{|G|v_g}{4\pi}$. The skyrmion effective velocity is $\mathbf{v}_e = \rho^2 \frac{\hbar \mathbf{q}}{m}$, where ρ is the SW amplitude, q is the magnitude of SW wave vector, and m is the magnon mass [34]. σ is the magnon scattering cross section of the skyrmion,

$$\left(\begin{array}{c} \sigma_{\parallel} \\ \sigma_{\perp} \end{array} \right) = \int_0^{2\pi} \left(\begin{array}{c} 1 - \cos \chi \\ -\sin \chi \end{array} \right) \frac{d\sigma}{d\chi} d\chi, \quad (15)$$

where χ is the scattering angle of the SW on the skyrmion and $\frac{d\sigma}{d\chi}$ is the energy-dependent scattering cross section. Usually, $\sigma_{\perp} \approx \frac{4\pi}{q}$ and $\sigma_{\parallel} \sim \frac{1}{q^2}$ [34,35]. The skyrmion Hall angle is $\beta = \arctan(\sigma_{\parallel} / \sigma_{\perp})$, so $f_{\text{scatter} \parallel} / f_{\text{scatter} \perp} = \tan \beta$. The parameter L_{mag} accounts for the attenuation of SWs by the Gilbert

damping according to

$$L_{\text{mag}} = \left(\alpha \sqrt{\frac{m}{2\hbar}} 2\pi f \right)^{-1}, \quad (16)$$

in which f is the SW frequency.

The way that SWs interact with the skyrmion can also be described in terms of transmission (T) and reflection (R) coefficients. We found that these quantities will change with time as the skyrmion moves, so we can expect that the force from SWs is not only based on the SW amplitude but also these changing interactions of the SW with the skyrmion: We can expect that $\mathbf{f}_{\text{scatter}}$ should depend on T and R . (The SW absorption coefficient is thus $A_{\text{sw}} = 1 - T - R$.)

For SWs propagating along the track (x direction) and perfect transmission through the skyrmion ($T = 1$), the magnons must change their spin after passing through the domain wall at the skyrmion edge, and so transfer angular momentum to the local magnetization, giving rise to a STT on the magnetization at that point [13]. In the Thiele approach of regarding the skyrmion as a particle, this torque gives rise to a force that leads to a skyrmion velocity $\frac{-\rho^2}{2} \mathbf{v}_g$, where $\mathbf{v}_g = 2\gamma_0 A_{\text{ex}} \mathbf{q}$ is the SW group velocity, in which $\gamma_0 = 2\gamma / (\mu_0 M_s)$. The total force component in the SW propagation direction will only come from this STT between fully transmitted SW magnons and the skyrmion. While this idea was developed for a one-dimensional domain wall [13], where the force from transmitted SW will simply align with the x axis, here we generalize it to a two-dimensional skyrmion. Thus, we need to consider the component of $\mathbf{f}_{\text{transmit}}$ perpendicular to the SW propagation direction. This force on the skyrmion arising from STT can be written as

$$\mathbf{f}_{\text{transmit}} = f_{\text{transmit} \parallel} \hat{\mathbf{x}} + f_{\text{transmit} \perp} \hat{\mathbf{y}}, \quad (17)$$

which leads to

$$\begin{aligned} -4\pi f_{\text{transmit} \perp} + \alpha \mathbb{D} f_{\text{transmit} \parallel} \\ = (G^2 + \alpha^2 \mathbb{D}^2) v_x = \frac{-\rho^2 v_g (G^2 + \alpha^2 \mathbb{D}^2)}{2}, \end{aligned} \quad (18)$$

where the ratio between $f_{\text{transmit} \parallel}$ and $f_{\text{transmit} \perp}$ is set as $\tan \beta$ [35] and $f_{\text{transmit} \parallel}$ is in the negative on x direction, as shown in Fig. 1.

When the distance between the skyrmion and sample edge is a few times larger than l_{edge} , as is the case initially, \mathbf{f}_{edge} is negligible, and the forces on the skyrmion and the resultant skyrmion velocity are as shown in Fig. 1(a). First, we consider the case where the SWs are reflected by the skyrmion but not stronger than the transmitted SWs, and the transmitted SWs exert spin-transfer torque upon it [27]. Part of the torque's effect can be regarded as a longitudinal force $f_{\text{transmit} \parallel}$ from transmitted SWs on the skyrmion particle, which yields a retrograde motion of the skyrmion by reference to Eq. (18), as shown in Fig. 1(a). There is, in addition, a transverse force component $f_{\text{transmit} \perp}$, meaning that the retrograde motion is not exactly back along the track towards the SW source, but at an angle.

On the other hand, when the strong reflection of the SWs from the domain wall at the edge of the skyrmion is taken into account, an additional longitudinal force arises, owing to the

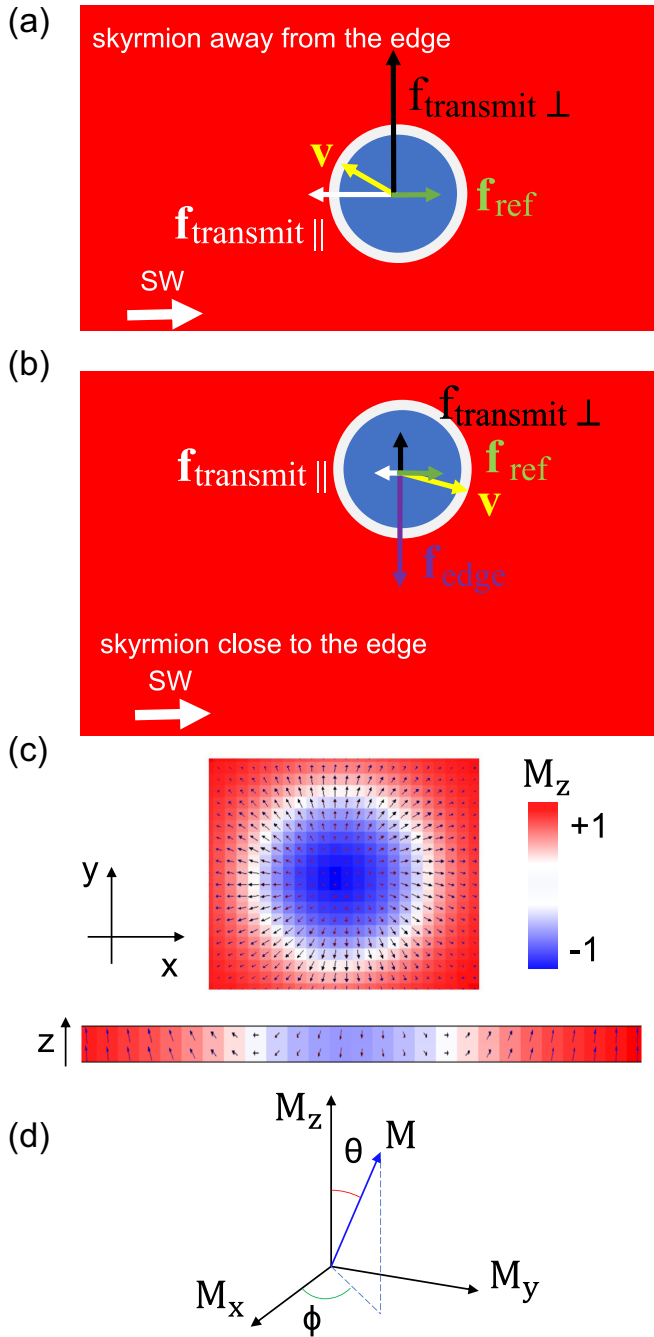


FIG. 1. Spin-wave driving forces for $Q = -1$ skyrmion. (a) When a free skyrmion experiences all the forces from impinging spin waves and the force from reflected spin waves is too small overcome the effect from $\mathbf{f}_{\text{transmit}}$ and $\mathbf{f}_{\text{scatter}\perp}$, the skyrmion's longitudinal velocity component is opposite to the spin-wave propagation direction. (b) Assuming the same transmitted SW is reduced, $\mathbf{f}_{\text{transmit}}$ can be overcome by \mathbf{f}_{ref} and/or the skyrmion is near enough to the track edge to experience edge repulsion, the additional force arising from linear momentum transfer can change the sign of the net longitudinal force and hence also the sign of longitudinal component of the velocity. The \mathbf{v} is a unit vector pointing to the direction of the skyrmion velocity. (c) 2D diagram of skyrmion with 1D spin orientation. The bar under the skyrmion is a 1D section through the skyrmion along the x axis. (d) The magnetization unit vector in spherical coordinates.

linear momentum transfer from the reflected magnons [36]. If it exceeds the force arising from the STT, it will be strong enough to change the sign of the net longitudinal component of the force on the skyrmion, and so change the skyrmion velocity to be positive along the x axis.

Another possible mechanism to obtain forward motion is to consider the perpendicular force from the edge, the transverse component of which can give skyrmion forward motion, as shown in Fig. 1(b). Such edge-induced torques can be very large [37].

To determine the effect of SW reflection, the excited magnon number density can be written as $n = \rho^2 M_s / (2\hbar\gamma)$, where ρ is the normalized SW amplitude. Since this is a volume density, to be able to apply it to the one-dimensional force calculation, we must multiply n by the cross-sectional area of the track. A skyrmion can be regarded as a circular reverse magnetic domain with a chiral domain wall between it and its surroundings. The spin orientations in a one-dimensional section along the central horizontal axis of such a skyrmion is a pair of domain walls, in this case of Néel form, as shown in Fig. 1(c) [38,39]. The magnetization unit vector can be expressed in spherical coordinates as shown in Fig. 1(d). The linear momentum of the left-hand-side domain wall of the skyrmion in this 1D section only has an x component given by $p_{\text{DW}} = M_s/\gamma \int \phi \sin\theta (\partial\theta/\partial x) dx = 2\Phi M_s/\gamma$, where θ is the angle between the magnetization and the z axis, and ϕ is the angle between the in-plane projection of the magnetization and x axis [as shown in Fig. 1(d)]. The domain-wall tilt angle $\Phi = \phi$ at the center of the domain wall [40]. Conservation of linear momentum then gives the force arising from the reflection of magnons,

$$\mathbf{F}_{\text{ref}} = \frac{d\mathbf{p}_{\text{DW}}}{dt} = -\frac{d\mathbf{p}_{\text{mag}}}{dt}, \quad (19)$$

where \mathbf{p}_{mag} is the linear momentum of the magnons. Considering only x components since that is the direction of magnon flow, we can then write

$$-\frac{dp_{\text{mag}}}{dt} = -nSv_g\delta p = -\frac{2M_s}{\gamma} \frac{d\Phi}{dt}, \quad (20)$$

where v_g is the magnitude of the SW group velocity, S is the cross-sectional area of the track, and the magnitude of the change in momentum is given by $\delta p = \hbar D_{\text{DMI}}/A_{\text{ex}}$ [13,36,40].

This means that

$$\frac{d\Phi}{dt} = -\frac{\rho^2 v_g \delta p}{4\hbar}, \quad (21)$$

and so

$$-\frac{dp_{\text{mag}}}{dt} = \frac{M_s \rho^2 v_g D_{\text{DMI}}}{2A_{\text{ex}} \gamma}, \quad (22)$$

and so

$$\mathbf{f}_{\text{ref}} = \left(\frac{\rho^2 v_g D_{\text{DMI}}}{2A_{\text{ex}} \mu_0 d_m}, 0, 0 \right). \quad (23)$$

\mathbf{f}_{ref} is a force that only has a component along the direction of magnon flow, defined here as the x axis. When $|\alpha \mathbb{D} f_{\text{ref}} R| > |\alpha \mathbb{D} f_{\text{transmit}} T|$, then $f_x > 0$. So, $-4\pi f_y = -4\pi (T f_{\text{transmit}\perp} + f_{\text{edge}})$ will be more likely be positive when approaching the upper edge, and the longitudinal component of the skyrmion

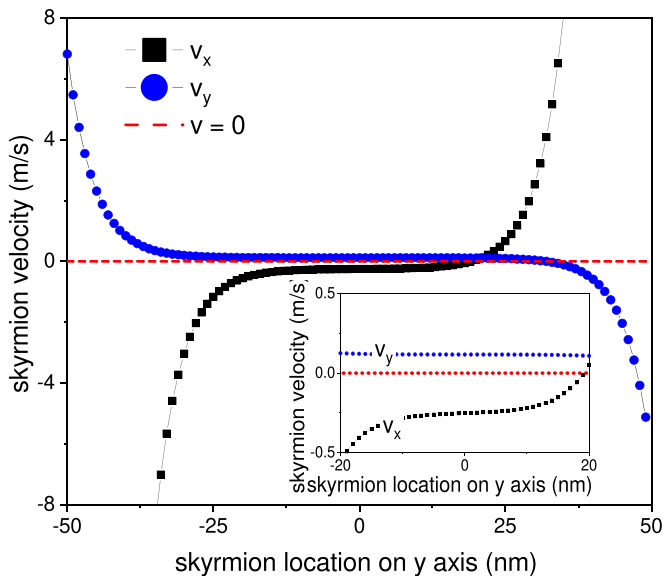


FIG. 2. Initial skyrmion velocity decomposed into x and y components for different initial positions on the y axis across a 100-nm-wide track. Spin waves are propagating in the in $+x$ direction along the track. Note that the initial velocity in the down track direction x depends on which half of the track the skyrmion starts in. The inset is a magnification of the central region of the main plot.

velocity will be $v_x > 0$. When the transmission of SWs is reduced, or the reflection of SW or α grows, the skyrmion will be more likely to move along the SW propagation direction.

In the work we present, the x component of the force on the skyrmion becomes

$$|f_x| = |(Tf_{\text{transmit}}| + Rf_{\text{ref}})e^{\frac{-x}{L_{\text{mag}}}}|. \quad (24)$$

Assuming that \mathbf{f}_{mag} is fixed at a given x -axis location, the initial x and y components of the skyrmion velocity, calculated using Eqs. (7) and (8), are shown in Fig. 2 for different starting positions across a 100-nm-wide track, with values based on the simulation parameters described in Table I in the next section and fixed representative values of $R = 0.2$ and $T = 0.8$.

The results illustrate the importance of the gyrotropic motion and edge forces. For starting positions closer to the upper edge of the track (larger positive y), the stronger the edge repulsion force pointing in the $-y$ direction will be on the skyrmion, and so the gyrotropic effect on the skyrmion will lead to the skyrmion moving along the SW propagation direction $+x$. On the other hand, the closer to the lower edge, the stronger the edge repulsion force pointing in the $+y$ direction

TABLE I. Micromagnetic parameters representing typical values for an experimental sample.

Parameter	Symbol	Value	Unit
Saturation magnetization	M_s	1.004	MA/m
Exchange stiffness	A_{ex}	3.6	pJ/m
Anisotropy constant	K_u	1.0	MJ/m ³
DMI constant	D_{DMI}	1.5	mJ/m ²

skyrmion will be, causing the skyrmion to move against the SW propagation in the $-x$ direction.

When the skyrmion is initially located at $y = 20$ nm, the initial skyrmion velocity $v_x = 0$, while v_y is positive. Once the skyrmion moves on the y axis, the balance between gyrotropic and dissipative terms is broken and the skyrmion will have a finite velocity on the x axis.

For starting positions close to the top edge, the skyrmion has a negative velocity on the y axis arising from the strong repulsive force from the edge, but it will still have a positive velocity on the x axis. In the simulations we shall present in the following sections, the initial skyrmion locations are all set to be 0 nm, the center of the track, where initial motion is towards the upper edge. Thus, we only ever observe the skyrmion going down and forward in narrow track after long simulation times after the skyrmion has been traveling along the upper edge for some time.

We report micromagnetic simulations that show the presence of skyrmion transient retrograde motion with varying sample widths and damping constant. We exploit values of the reflected and transmitted SW intensity determined from the simulated magnetization data to evaluate the changes of R and T for the SWs during the motion of the skyrmion and how they lead to the observed dynamics on the basis of the framework developed in this section.

III. MICROMAGNETIC SIMULATIONS

We have performed numerical micromagnetic simulations using the OOMMF package [25]. The simulation cell dimensions were set to [1 nm, 1 nm, 0.4 nm]. The magnetic track thickness $d_m = 0.8$ nm. We simulated wires with a length of 1000 nm and variable width w in the range 40–100 nm. The track geometry is depicted in Fig. 3. The value of α was selected for each sample from the range [0.02, 0.06], but in the regions close to the ends of the track we set $\alpha = 1$ so the SWs are not reflected back along the track. The materials parameters used are based on the representative magnetic properties of a [Ta/Pt/Co₆₈B₃₂/Ir/Pt] sheet film prepared in our laboratory and are shown in Table I.

The initial magnetization was fully saturated normal to the x - y plane. The SWs were excited by applying a time-dependent magnetic field $H_0 \sin(2\pi ft)$, directed along the y axis, where $\mu_0 H_0 = 800$ mT is the amplitude of the exciting field and $f = 80$ GHz is the frequency. The frequency of the SWs will be the same as the exciting field. The excitation field is localized to one column of cells located at $x = -150$ nm.

To obtain the dispersion relation $f(q)$ of the SWs, shown in Fig. 3(b), sine pulses of varying frequency were applied to the track which was in a static saturating field of $\mu_0 H_z = 100$ mT. The magnetization data was used as the input signal to a discrete Fourier transform process to obtain the wave vector k [41]. The magnon mass calculated from this SW dispersion relation is $m = 2.41 \times 10^{-29}$ kg [34].

To study SW-driven skyrmion motion, we first stabilized a skyrmion spin texture. A static external field H_z is applied on the whole sample along the z axis. A Néel-type skyrmion was nucleated and relaxed at the center of the track where $x = 0$. The equilibrium diameter found after this procedure is 17 nm. The SW excitation was then switched on with $f = 80$ GHz.

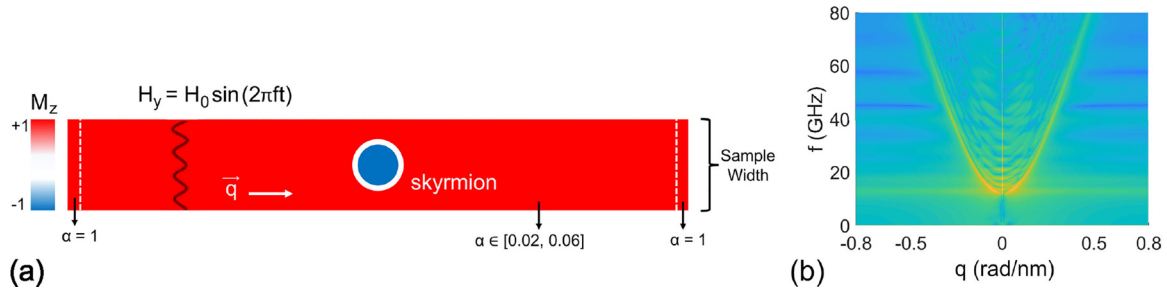


FIG. 3. Spin-wave excitation in a magnetic track. (a) The sample geometry simulated in OOMMF, with a red-blue color scheme used to depict the z component of the magnetization. The track is 1000 nm long and of variable width w . The damping constant α is set to 1 in 10-nm-long regions at the ends of the track to avoid spin-wave reflections and takes variable values in the range 0.02–0.06 in the main part of the track for different simulations. A skyrmion, shown schematically, is initialized at the center of the track at $x = 0$ nm. The spin-wave excitation field is localized at a position $x = -150$ nm with time dependence $\mathbf{H}_y = H_0 \sin(2\pi ft)\hat{y}$. (b) The dispersion relation $f(q)$ for spin waves in the 100 nm width and $\alpha = 0.03$ nano track, showing the expected parabolic form.

SWs propagate away from the excitation region along the x direction, driving the motion of the skyrmion when they reach it.

IV. SIMULATION RESULTS

A. Retrograde motion of skyrmions in wide tracks

A SW that is propagating along the x axis induces skyrmion motion, as shown in Fig. 4(a). The skyrmion displacement along the x direction, Fig. 4(b), and the y direction, Fig. 4(c), as a function of simulation time with different track widths in the range $w = 40$ –100 nm with a 0.1 ns time step. These simulations were carried out with the Gilbert damping set to $\alpha = 0.02$.

When the track is narrow, $w \lesssim 50$ nm, the skyrmion is driven along the propagation direction of SW as shown in the $w = 40$ nm example of Fig. 4(a). In this case, the x component of the skyrmion velocity is always positive.

For wider tracks, the motion is more complex, as shown for the $w = 90$ nm example depicted in Fig. 4(a). The skyrmion shows negative initial velocity along x . The skyrmion also has a y component of velocity, since the gyrotropic motion will also lead to the skyrmion moving toward the upper edge, as seen in the 90-nm track width example shown in Figs. 4(a) and 4(c) [8,42]. The transient retrograde motion stops when the skyrmion approaches the track edge after a few tens of ns, and the skyrmion then begins moving along the edge in the positive x direction. The skyrmions will have to move up further to reach the track edge before changing directions for the wider tracks, as shown in Figs. 4(b) and 4(c). As the theory based on the SW scattering on skyrmion shows in Eqs. (7) and (14), $\mathbf{f}_{\text{scatter}}$ always drives the skyrmion towards the SW source on a borderless sample. The skyrmions all move towards the top edge until the distance between the skyrmion center and the upper edge is around 25 nm before starting to have positive velocity on the x axis.

Close to the sample edges, the presence of D_{DMI} gives rise to a twist in the magnetization away from the z axis [26]. As an example, the z component of the magnetization for the 100-nm-width sample in the notionally uniform state (i.e., without a skyrmion) is shown in Fig. 5. A canting away from the z direction is visible that extends for a few nm into the

track from its edge. This twisting gives rise to the edge force \mathbf{f}_{edge} discussed in Sec. II above, with the twist extending in from the edge by a distance L_{edge} . A value of $L_{\text{edge}} = 2.4$ nm is calculated from D_{DMI} , A_{ex} , and the other magnetic properties of track using Eqs. (10) and (12) [33]. The OOMMF simulation results also give a magnetization that depends exponentially on position, shown in Fig. 5, with the fit in the inset of that figure yielding $L_{\text{edge}} = 1.5$ nm, which is of the same order of magnitude. The small difference can be accounted for by the fact that demagnetizing effects are properly accounted for in the numerical simulation but neglected in the analytical formulas.

The sum of the radius of skyrmion and L_{edge} is close to 10 nm. This means when the distance between the skyrmion center and track edge is smaller than ~ 10 nm, the skyrmion starts to feel the influence of \mathbf{f}_{edge} . This force acts in the y direction and so we see that the edge force will give rise to a positive term in v_x as given by Eq. (7). If this additional force is large enough, it will overcome $\mathbf{f}_{\text{transmit}}$ [similarly to what is shown in Figs. 1(a) and 1(b)] and hence the skyrmion will start moving forward once it reaches the track edge [43]. In a wider track, the skyrmion will take more time to reach the edge region where this force can be active, so we can expect a larger transient retrograde motion of the skyrmion towards the SW source before the forward motion sets in.

B. Retrograde motion of skyrmion with enhanced damping

Fixing the sample width at $w = 100$ nm, we ran a similar series of simulations in which we varied the value of α in the range [0.02, 0.06] with a 0.1 ns time step. The resulting skyrmion displacements in the x direction as a function of simulation time with varying damping constant are shown in Fig. 6(a). When $\alpha = 0.02, 0.03$, or 0.04 , we again see that the skyrmion initially moves backwards against the SW direction. The skyrmion only has a positive initial velocity when the track has $\alpha \geq 0.05$. As shown in Fig. 6(b), the skyrmions still have a velocity in the y direction due to the skyrmion Hall effect. The distance between the skyrmion and the edge when the skyrmion moves away from the SW source is smaller when α is stronger.

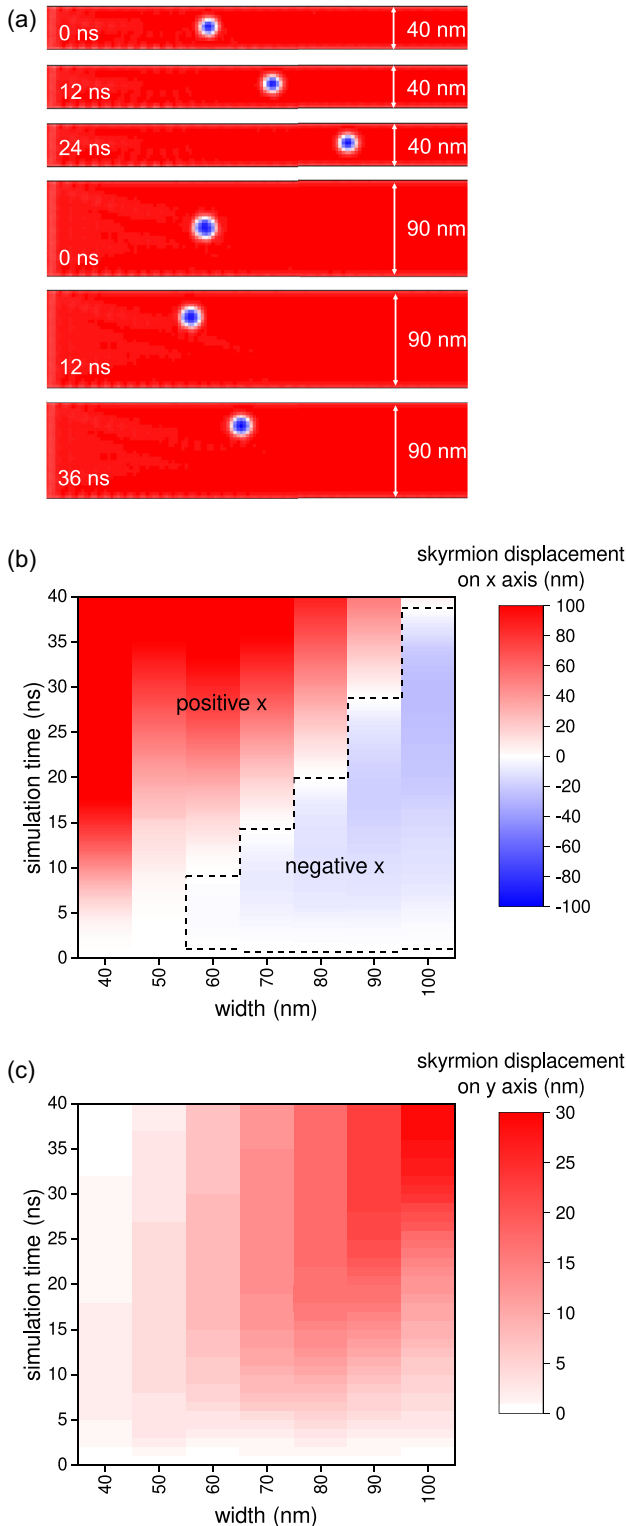


FIG. 4. Spin-wave-driven skyrmion motion. (a) Snapshots at different simulation times of samples with track widths = 40 nm and 90 nm. Time-dependent skyrmion displacement on the (b) x direction and (c) y direction for various magnetic track widths in the range 40–100 nm. The region enclosed by the dashed line in (b) is where the skyrmion x displacement is negative with respect to the starting position.

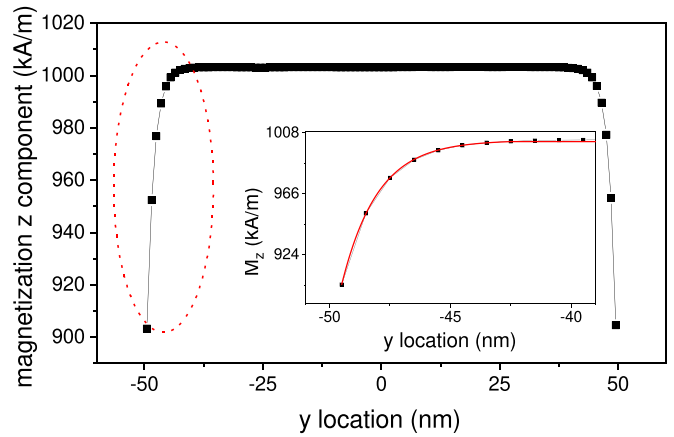


FIG. 5. Out-of-plane component of magnetization M_z across the track width direction (y axis) for the $w = 100$ -nm-wide track. The inset graph shows that the z component of magnetization depends exponentially on distance from the edge, with a fit to $M_z = M_s - M_c \exp[-(x - \frac{w}{2})/L_{\text{edge}}]$ in the range $[-50 \text{ nm}, -40 \text{ nm}]$ region, where M_c is half the largest difference between the twisted magnetization and the saturation magnetization.

Assuming the skyrmion has the same R and T at the same position of each simulation, the strength of \mathbf{f}_x only depends on the amplitude of the SWs. A larger value of α leads to stronger attenuation of the SWs, owing to the shortening of L_{mag} , as described by Eq. (16). This reduces the force arising from the SW magnons for a fixed given distance between the skyrmion location and the SW source. Thus, it is easier for \mathbf{f}_{edge} to overcome the negative terms of the \mathbf{v}_x when the skyrmion is in a sample with larger α . In the real experiment, the skyrmion will be expected to show a simple forward motion because α of real thin cobalt alloy samples is usually much larger than 0.05 [44–47].

C. Time dependence of skyrmion motion induced by transmitted and reflected spin waves

We repeated the simulation in Fig. 6 with a finer time step of 5 ps for $w = 40 \text{ nm}$ and $w = 100 \text{ nm}$, setting $\alpha = 0.03$, to study the SW transmission through and reflection from the skyrmion as a function of time. As shown by the expression for the scattering force Eq. (14), the amplitude of the SW will exponentially decay along the track. The SW can be represented by picking out an in-plane component of the magnetization—here we use the y component—which yields a damped sine function in space, an example of which is plotted in Fig. 7. The expected damping length is $L_{\text{mag}} \approx 139 \text{ nm}$, based on a calculation using Eq. (16), close to the value of 101.7 nm obtained by fitting a damped sine wave to the M_y data.

In a similar manner, by extracting the in-plane magnetization data from the simulations (see Appendix A for details) and fitting a damped sine wave to them, we can obtain the SW amplitude for any given region in the track. By selecting appropriate regions of the track, we have done this for three cases: The transmitted SW that has passed through the

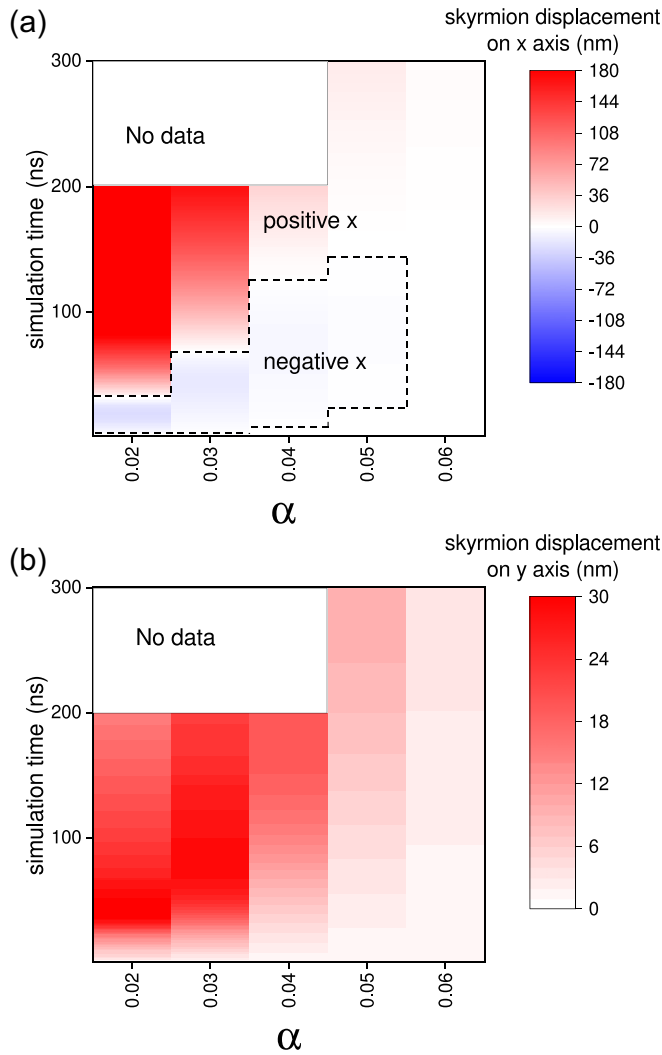


FIG. 6. Time-dependent (a) x -direction and (b) y -direction skyrmion displacement in a $w = 100$ nm track for various values of the Gilbert damping constant in the range $\alpha = 0.02$ – 0.06 . The region enclosed by the dashed line in (b) is where the skyrmion x displacement is negative and the region enclosed by the black line doesn't have data since no simulations were done for those ranges of parameters.

skyrmion, the SW reflected from the skyrmion, and, for comparison, the same frequency spin wave in the same region in an empty—i.e., no skyrmion—track. The attenuation caused by L_{mag} depends on the distance between the data collection region and the source of the SWs. By comparing the transmitted SW amplitude in the presence of the skyrmion with that in an empty track we can obtain the transmission coefficient (T). Similarly, we can determine the reflection coefficient (R) for SWs by comparing the amplitudes with and without the skyrmion in the region before the SWs reach it. Each process can be done at a certain simulation time.

In our simulations, the skyrmion starts in the center of the track and so always moves toward the sample upper edge because of the skyrmion Hall effect (see Fig. 2). We define the distance between the skyrmion center and the sample upper edge $d_{\text{se}} = \frac{w}{2} - y$. [This distance determines the exponential edge force term related to the top edge in

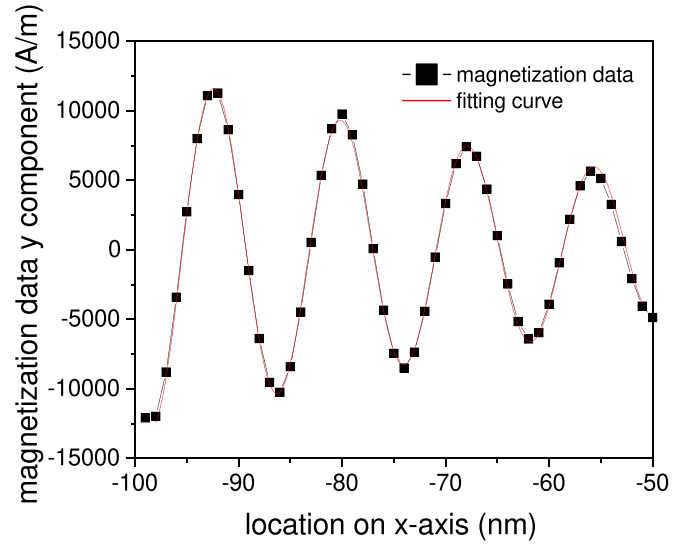


FIG. 7. The y component of magnetization shows a damped spin wave along the propagation direction. The red line is the result of fitting a damped sine wave of the form $M_y = M_{y_0} + I \exp(-x/L_{\text{mag}}) \sin(q(x - x_0))$, where I is an amplitude and x_0 is a spatial phase. The fit returns a value $L_{\text{mag}} = 101.7$ nm and wave vector $q = 0.52$ rad/nm. The range of x -axis locations shown here is in the area of the spin-wave source at $x = -150$ nm and the starting position of the skyrmion at $x = 0$.

Eq. (9), represented by the orange gradient in Fig. 8.] We show the time dependence of d_{se} for both the $w = 40$ nm and $w = 100$ nm track is shown in the Fig. 8. We find that the repulsion becomes too strong for the skyrmion to ever get closer than $d_{\text{se}} \sim 17$ nm to the edge. This leads to an effectively forbidden region for the skyrmion for $d_{\text{se}} < 17$ nm, which we subsequently show with red shading.

Both T and R vary during the simulation because they correlate with d_{se} , as shown in Fig. 9. (Their time dependence is shown in Appendix B.) Only the data related to the skyrmions' first approach to the sample edge is plotted. (At longer times, they rebound slightly from the edge, seen here for the

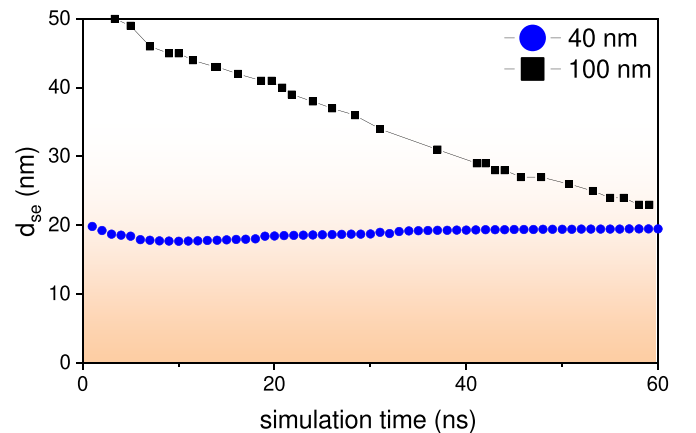


FIG. 8. Time dependence of the distance between skyrmion center and the upper edge d_{se} for the $w = 40$ nm and $w = 100$ nm simulations. The orange gradient represents the region in which the skyrmion starts to experience a noticeable repulsive force from the upper edge.

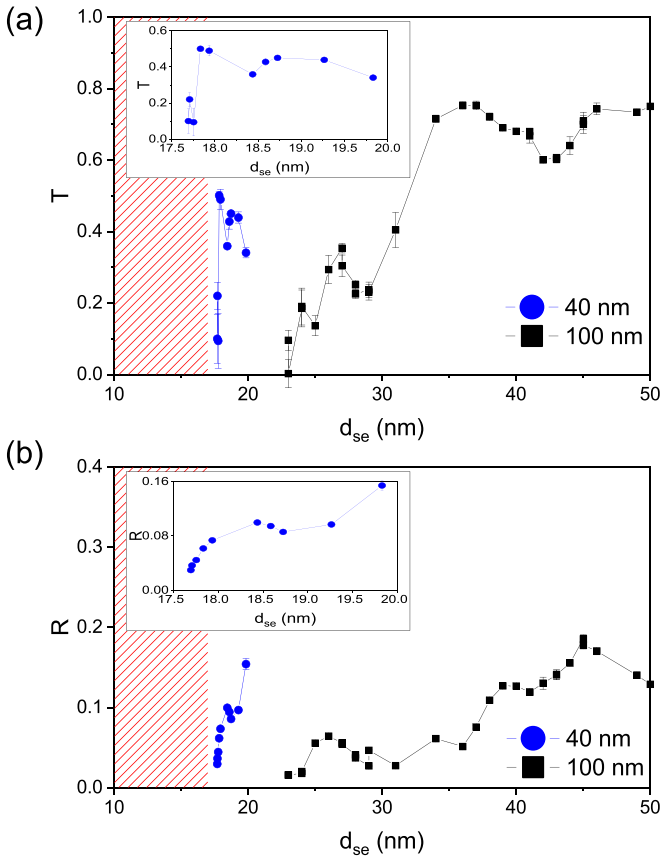


FIG. 9. (a) T and (b) R of spin waves as a function of d_{se} for a simulation with $w = 100$ nm and $w = 40$ nm. The shaded red region is where the skyrmion cannot overcome the repulsive force edge force and so is effectively forbidden in these simulations.

$w = 40$ nm trace in Fig. 8.) As d_{se} shrinks, a drop in both (a) T and (b) R are seen. The inset graph shows a zoom of the $w = 40$ nm trace. For the $w = 100$ nm case, T initially takes a high value of ~ 0.7 and starts to drop once d_{se} falls below about 35 nm. Presumably owing to the proximity to the edge, T for the $w = 40$ nm case starts at a lower value ~ 0.5 , but also drops rapidly as the edge is approached. T eventually falls to almost zero in both cases. Although not starting at such a high level, there is a similar finding for R , which also drops and reaches a value close to zero as the skyrmion comes to its point of closest approach to the edge.

These changes in the way that SWs interact with the skyrmion suggest that it is not a perfectly rigid object with unchanging properties. To probe this further, we have measured the skyrmion diameter during each of our simulations, with the results shown in Fig. 10. Here we define the diameter as the distance between the extrema of the spatial derivative of M_z , as shown in the inset of Fig. 10. We can see that the skyrmion diameter shrinks as the edge is approached, presumably under the influence of the edge force. This change in skyrmion geometry could account for the change in the values of T and R .

We can see from Eq. (24) that the force f_x on the skyrmion is expected to have a term that is $\propto -T$ and another that is $\propto R$. Thus, we expect these changes in the way that the

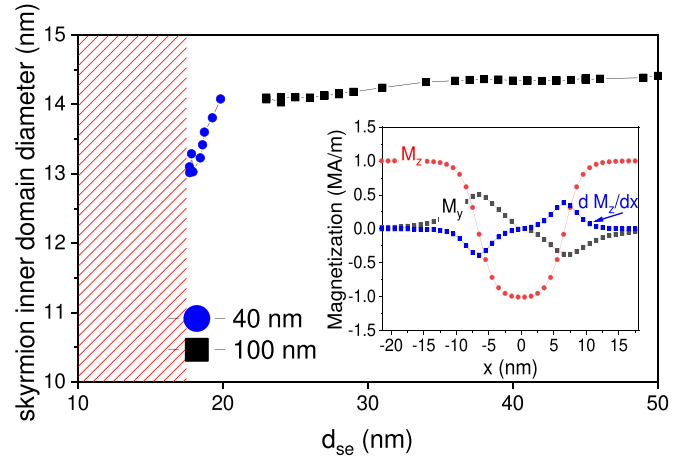


FIG. 10. Skyrmion inner domain diameter as a function of d_{se} on 100-nm and 40-nm-wide samples. The inner domain size is defined as the distance between the two extrema of $\frac{dM_z}{dx}$, as shown in the inset. The shaded red region is where the skyrmion cannot overcome the repulsive force edge force and so is effectively forbidden in these simulations.

skyrmion affects SWs to lead to changes in its dynamics. In the insets of Fig. 11, we show the time dependence of v_x for each of our two simulations as red solid circles.

As shown in the inset graph of Fig. 11(b), for the $w = 40$ nm track, the skyrmion initially accelerates as it approaches the upper edge before 10 ns and later its velocity drops again as it moves away from that edge, based on the d_{se} data shown in the Fig. 8. In this case, the value of T drops when d_{se} is smaller than 18 nm, as that edge is most closely approached. R also decreases similarly. Nevertheless, the skyrmion is always in the region that has strong f_{edge} , owing to the narrowness of this track, which means it always moves away from the SW source with positive v_x .

Meanwhile, for the $w = 100$ nm track, from Figs. 6 and 11(a), we can see that the skyrmion's initial backwards velocity starts to drop at around 30 ns. The skyrmion then begins to move in the forward direction at 43 ns, corresponding to the time that d_{se} is ~ 35 nm as shown in Fig. 8 and the drop in T takes place as shown in Fig. 9(a). The Thiele Eq. (7) and Eq. (24) show that the transmission of SWs will give rise to a force that pulls the skyrmion towards the SW source owing to the transfer of angular momentum.

On the other hand, the force owing to linear momentum transfer from reflected SW magnons can give rise to motion along the SW propagation direction as shown in Eq. (24). Surprisingly, the reflection coefficient R is not equal to $1 - T$, and it has a similar time dependence to T . For the 100-nm-wide track, R starts at a value of $R \approx 0.2$ before declining quickly once d_{se} is less than 40 nm, as shown in Fig. 9(b). Thus, this change in R cannot explain the change in direction of the skyrmion in the 100-nm-wide track, since R would need to rise to push the skyrmion away from the SW source by linear momentum transfer.

So far, in Sec. II and Eq. (7), when $4\pi Qf_{edge} + \alpha Df_x > 0$, $v_x > 0$. To compare this analytical prediction with our numerical simulation results, we insert Eq. (24) into Eq. (7)

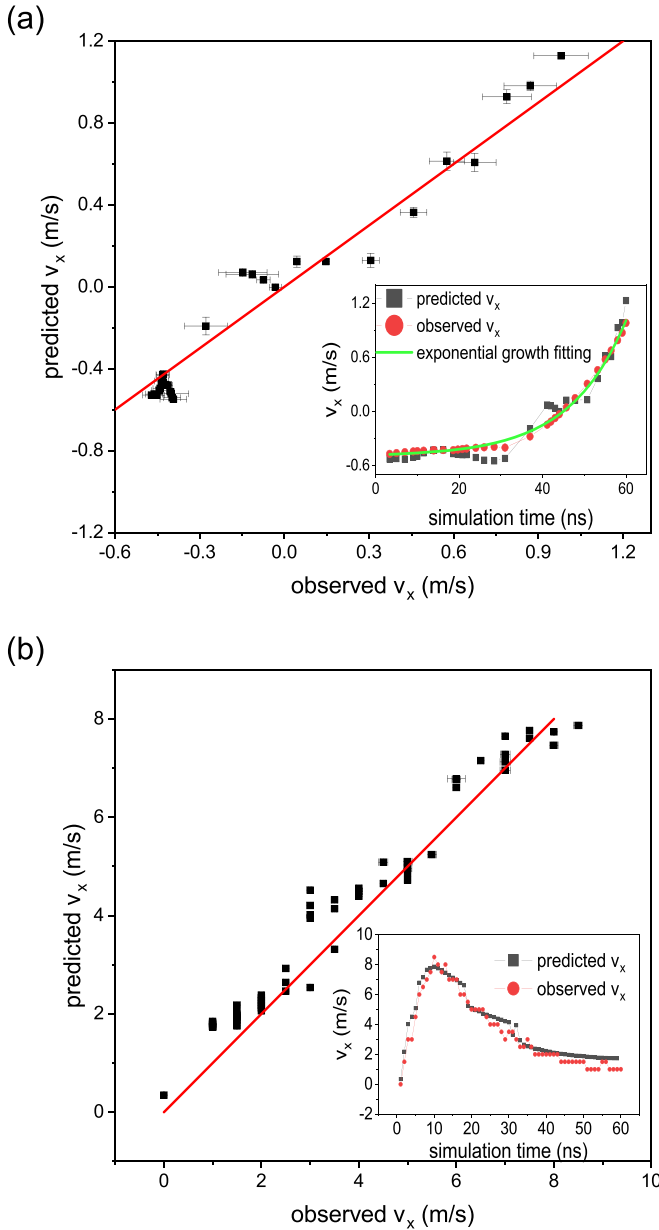


FIG. 11. The relationship between skyrmion velocity predicted by the Thiele equation and the velocity observed in the numerical simulation of (a) 100-nm-wide track and (b) 40-nm-wide track. The data points can be compared with the red line of unity slope. Insets show the two velocity data sets each as a function of simulation time. The velocity observed in the $w = 100$ nm numerical simulation was fitted with an exponential of the form $v_x = v_0 + v_i e^{(t-t_0)/\tau}$ shown as a solid green line. Here, v_0 is the initial velocity, v_i is a velocity prefactor for the time dependent part, and τ is a characteristic timescale.

to obtain

$$v_x = \frac{4\pi Q(f_{\text{edge}} + T f_{\text{transmit}\perp}) + \alpha \mathbb{D} f_x}{(\alpha \mathbb{D})^2 + G^2}. \quad (25)$$

We then input the time-dependent values of T and R into the Thiele equation calculation and plot the results as black solid squares as a function of time in the insets of that figure.

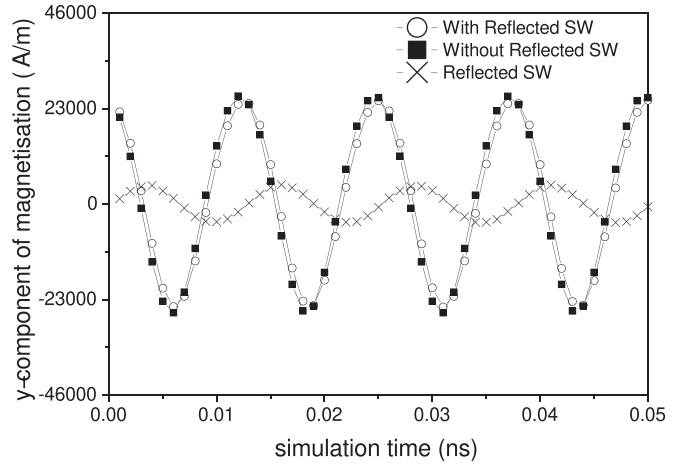


FIG. 12. The y component of magnetization at $[x_s - r_s, y_s]$ of skyrmion during an interval of 0.05 ns shows the spin wave along the propagation direction; the difference of magnetization data with and without skyrmion is the reflected spin wave.

We calculated the prefactor \mathbf{f}_0 of \mathbf{f}_{edge} to be 2977 m/s by using Eq. (11), and $f_{\text{scatter}\perp}$ without any SW damping factor to be around 274 m/s. $L_{\text{edge}} = 2.5$ nm and $L_{\text{mag}} = 139$ nm, by using Eqs. (12) and (16), respectively. $\mathbb{D} = \frac{d\pi^3}{2\gamma_{\text{DW}}}$ [8], in which d is the skyrmion diameter and γ_{DW} is the domain wall width at the skyrmion edge.

The observed skyrmion velocity in the 100-nm-wide track rises rapidly, with a very good fit to an exponential (green line) for times before about 25 ns and after 45 ns, as shown in Fig. 11(a). \mathbf{f}_{ref} and $\mathbf{f}_{\text{transmit}}$ decay after 30 ns as the skyrmion has a velocity on the y axis towards to the upper edge because of the gyrotropic effect from f_x , as shown in Figs. 2 and 8. Since \mathbf{f}_{edge} is exponential in skyrmion position y according to Eq. (9), the strongest force term in the Thiele equation is the exponentially growing \mathbf{f}_{edge} , which leads to exponential growth in the velocity along x through Eq. (7).

These predicted velocities based on Eq. (25) are plotted against those directly observed in the simulations in the main panels of Fig. 11. The black scatter data are generally in good agreement with a line of unity slope, drawn in red: Overall, the predictions of inserting T and R into the Thiele formalism compare well with the velocity taken directly from the simulation.

In Fig. 11(a), there is excellent agreement between the two data sets for two regimes: (i) when the skyrmion is undergoing its initial retrograde motion for $v_x \sim -0.5$ m/s up to a simulation time of ~ 25 ns and (ii) when the skyrmion is undergoing acceleration along the track edge at long simulation times after ~ 45 ns, when $v_x \gtrsim 0.4$ m/s. This shows that the underlying physical picture for v_{x1} , which only considers the strength of T and R on \mathbf{f}_x , gives a good description in these regimes. The agreement is poorer, but still fair, for intervening data points around the point where the skyrmion reverses direction, and potentially other physics may be at play there.

This leads us to propose a form for $f_x = T f_{\text{transmit}\parallel} + R f_{\text{ref}}$ and $f_y = f_{\text{edge}} + T f_{\text{transmit}\perp}$ that replaces f_{scatter} . However, using Eq. (7) to predict the skyrmion velocity means that the

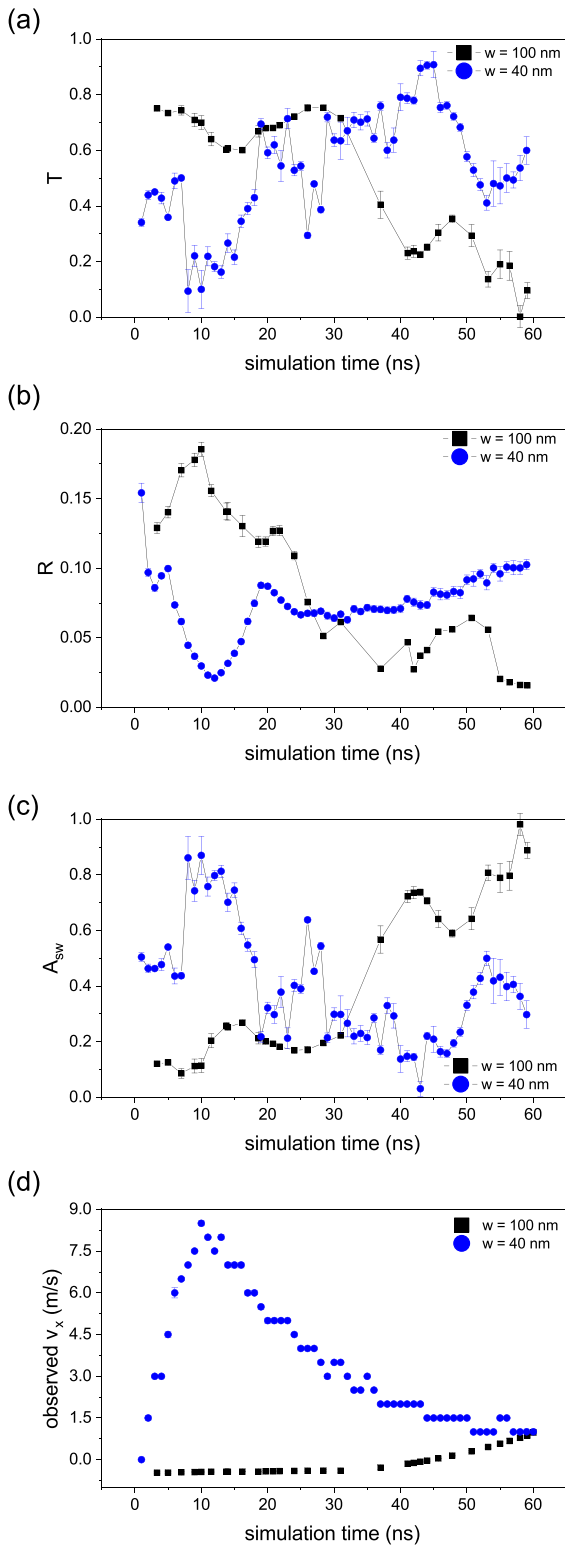


FIG. 13. The variation of T , R , A_{sw} and skyrmion velocity with simulation time.

terms for the force arising from the absorption of SWs are neglected since it is challenging to get a precise energy for skyrmion motion from the total absorbed SW energy. So, before 50 ns, the calculated result does not work well when the skyrmion is still far away from the edge and close to the

SW source. When the skyrmion is close to the edge, f_{edge} is much stronger than the SW force in terms of its effect on the skyrmion velocity, and the calculated results are in good agreement with the ones extracted directly from the numerical simulation.

In Fig. 11(b), there is also excellent agreement between the two data sets. This is the case both when the skyrmion is accelerating and moving away from the SW source because of the short distance between the skyrmion and upper edge in the initial state, and also when the skyrmion velocity is decreasing as it is pushed away from the upper edge. In the latter case, the skyrmion is gaining less f_{edge} and force from the SW because of the longer distances involved, and so the force balance leads a stable velocity of skyrmion.

If the damping constant is larger than 0.03, the SW amplitude will attenuate more rapidly and the term f_y in Eq. (7) will more easily overcome the negative term of f_x . This fact can explain the shape of the contour of α dependent skyrmion displacement in Fig. 6. For wider samples, the skyrmion will need a longer time to reach the region where the edge forces are significant, and so further negative displacement will show up in the contour plot of the sample width-dependent skyrmion displacement in Fig. 4.

V. CONCLUSION

In conclusion, we have studied the SW-driven motion of skyrmions in a nanoscale track by means of time-dependent micromagnetic simulations and found a range of conditions where there is a transient retrograde motion of the skyrmion. Our results show that the skyrmion will have retrograde motion towards the SW source at the onset of its movement when the track has a large enough width and a low damping constant, but the skyrmion always moves away from the SW source at long simulation times. We cross-checked the simulated skyrmion velocity with the results of the Thiele equation and find qualitatively similar skyrmion motion from the calculation but also find that only using reflection and transmission data cannot give a fully quantitative relationship between calculated velocity and simulated velocity. The gyrotropic term in the Thiele equation is not negligible, and the repulsive force from the sample edge also affects the skyrmion velocity by this means. We suggest that also considering the absorption of SW magnons is a possible way forward in the future.

The simulation results give a possible motion of skyrmion that might be observed in future experiments. The force from the track edge is a potential means to adjust the skyrmion motion. A higher damping sample (e.g., a CoB alloy thin film [44]) will have a shorter retrograde distance than a low damping sample ($\alpha < 0.05$ for simulation magnetic properties), as can be seen from Fig. 6. Moreover, if the initial position of a skyrmion in y is not well controlled, then the motion along the x direction will not be deterministic, since the time taken for the skyrmion to reach the near-edge region and experience the edge forces will be unpredictable.

The OOMMF input files and data associated with this paper are openly available from the University of Leeds Data repository at [48].

ACKNOWLEDGMENTS

We acknowledge Joseph Barker for constructive discussions and help in setting up the OOMMF software in a high-performance computer environment.

APPENDIX A: AMPLITUDE OF SPIN WAVES

To determine the amplitudes of the SWs that are propagating in the track we simulated, we analyzed the data arrays output at each 5 ps time step of the simulation, which contains the three components of the magnetization within each [1 nm, 1 nm, 0.4 nm] cell. An example of plotting the y component of magnetization as a function of x was already given in Fig. 5, showing a damped sine wave. Simulations of the SW propagation both with and without the skyrmion on the track were carried out.

Analysis of the former yields the coordinates of the skyrmion location in the track as $[x_s, y_s]$. The y -component magnetization data from 50-nm-long regions which have the same y location as the skyrmion but are 100 nm downstream from it, i.e., from x_s+100 nm to x_s+150 nm, were fitted with damped sine functions $M_y = M_{y_0} + I \exp(-x/L_{\text{mag}}) \sin(q(x - x_0))$, where I is the amplitude of the SW at the location $[x_s+100$ nm, $y_s]$, q is the SW wave number, M_{y_0} is the amplitude offset, and x_0 is a phase

shift. The ratio between the values of I with and without the skyrmion is the transmission coefficient T .

Determining the reflection coefficient R required a different approach since plotting the spatial dependence on the waveform upstream of the skyrmion yields a complex interference pattern between the incident and reflected waves. We therefore select a point in space at location $[x_s(t) - r_s(t), y_s(t)]$, where r_s is the skyrmion radius and the variation of the y component of magnetization for a 1 ns time interval (200 data points) are determined, again for the system with and without the skyrmion. An example is shown in Fig. 12. Taking the data without the skyrmion as the pure incident waveform, we can subtract it from the data without the skyrmion to yield the reflected wave. Both the reflected SW and SW without skyrmion on the track are fitted with sine functions $a \sin(\omega t + \theta) e^{-t/\epsilon}$ to yield their amplitudes a . The ratio between the amplitudes of the reflected SW and the incident SW yields the reflection coefficient R .

APPENDIX B: TIME-DEPENDENCE OF T , R , A_{sw} AND SKYRMION VELOCITY

The relationship between the T , R , and d_{se} was shown in Fig. 9. In this Appendix, for completeness, we provide plots of T , R , A_{sw} , and skyrmion velocity as a function of simulation time for the first 60 ns simulation time in Fig. 13. We define the absorption $A_{\text{sw}} = 1 - T - R$.

-
- [1] N. Nagaosa and Y. Tokura, Topological properties and dynamics of magnetic skyrmions, *Nat. Nanotechnol.* **8**, 899 (2013).
- [2] A. Bogdanov and A. Hubert, Thermodynamically stable magnetic vortex states in magnetic crystals, *J. Magn. Magn. Mater.* **138**, 255 (1994).
- [3] A. Soumyanarayanan, M. Raju, A. L. Gonzalez Oyarce, A. K. C. Tan, M.-Y. Im, A. P. Petrović, P. Ho, K. H. Khoo, M. Tran, C. K. Gan, F. Ernult, and C. Panagopoulos, Tunable room-temperature magnetic skyrmions in Ir/Fe/Co/Pt multilayers, *Nat. Mater.* **16**, 898 (2017).
- [4] G. Finocchio, F. Büttner, R. Tomasello, M. Carpentieri, and M. Kläui, Magnetic skyrmions: From fundamentals to applications, *J. Phys. D: Appl. Phys.* **49**, 423001 (2016).
- [5] F. Jonietz, S. Mühlbauer, C. Pfleiderer, A. Neubauer, W. Münzer, A. Bauer, T. Adams, R. Georgii, P. Böni, R. A. Duine, K. Everschor, M. Garst, and A. Rosch, Spin transfer torques in MnSi at ultralow current densities, *Science* **330**, 1648 (2010).
- [6] J. Sampaio, V. Cros, S. Rohart, A. Thiaville, and A. Fert, Nucleation stability and current-induced motion of isolated magnetic skyrmions in nanostructures, *Nat. Nanotechnol.* **8**, 839 (2013).
- [7] S. Woo, K. Litzius, B. Krüger, M.-Y. Im, L. Caretta, K. Richter, M. Mann, A. Krone, R. M. Reeve, M. Weigand *et al.*, Observation of room-temperature magnetic skyrmions and their current-driven dynamics in ultrathin metallic ferromagnets, *Nat. Mater.* **15**, 501 (2016).
- [8] W. Jiang, X. Zhang, G. Yu, W. Zhang, X. Wang, M. B. Jungfleisch, J. E. Pearson, X. Cheng, O. Heinonen, K. L. Wang, Y. Zhou, A. Hoffmann, and S. G. E. te Velthuis, Direct observation of the skyrmion Hall effect, *Nat. Phys.* **13**, 162 (2017).
- [9] J. Zázvorka, F. Jakobs, D. Heinze, N. Keil, S. Kromin, S. Jaiswal, K. Litzius, G. Jakob, P. Virnau, D. Pinna, K. Everschor-Sitte, L. Rózsa, A. Donges, U. Nowak, and M. Kläui, Thermal skyrmion diffusion used in a reshuffler device, *Nat. Nanotechnol.* **14**, 658 (2019).
- [10] A. Tan, P. Ho, J. Lourembam *et al.*, Visualizing the strongly reshaped skyrmion Hall effect in multilayer wire devices, *Nat. Commun.* **12**, 4252 (2021).
- [11] X. Zhang, M. Ezawa, D. Xiao, G. P. Zhao, Y. Liu, and Y. Zhou, All-magnetic control of skyrmions in nanowires by a spin wave, *Nanotechnology* **26**, 225701 (2015).
- [12] X. Zhang, J. Müller, J. Xia, M. Garst, X. Liu, and Y. Zhou, Motion of skyrmions in nanowires driven by magnonic momentum-transfer forces, *New J. Phys.* **19**, 065001 (2017).
- [13] P. Yan, X. S. Wang, and X. R. Wang, All-Magnonic Spin-Transfer Torque and Domain Wall Propagation, *Phys. Rev. Lett.* **107**, 177207 (2011).
- [14] Y. Jiang, H. Y. Yuan, Z.-X. Li, Z. Wang, H. W. Zhang, Y. Cao, and P. Yan, Twisted Magnon as a Magnetic Tweezer, *Phys. Rev. Lett.* **124**, 217204 (2020).
- [15] P. Tengdin, B. Truc, A. Sapozhnik, S. Gargiulo, I. Madan, T. Schoenenberger, P. R. Baral, P. Che, A. Magrez, D. Grundler, H. M. Rønnow, T. Lagrange, and F. Carbone, Imaging the controllable rotation of a skyrmion crystal driven by femtosecond laser pulses, [arXiv:2110.04548](https://arxiv.org/abs/2110.04548).
- [16] X. Yu, F. Kagawa, S. Seki *et al.*, Real-space observations of 60-nm skyrmion dynamics in an insulating magnet under low heat flow, *Nat. Commun.* **12**, 5079 (2021).

- [17] L. Song, H. Yang, B. Liu, H. Meng, Y. Cao, and P. Yan, A spin-wave driven skyrmion diode under transverse magnetic fields, *J. Magn. Magn. Mater.* **532**, 167975 (2021).
- [18] L. Kong, L. Bo, R. Zhao, C. Hu, L. Ji, Y. Zhang, and X. Zhang, Linear dependence of skyrmion velocity on response resonance frequency of local magnetization, *Appl. Phys. Lett.* **116**, 192407 (2020).
- [19] R. Mansell, T. Schaffers, R. B. Holländer, H. Qin, and S. van Dijken, Interaction of propagating spin waves with extended skyrmions, *Appl. Phys. Lett.* **121**, 242402 (2022).
- [20] P. Yan, A. Kamra, Y. Cao, and G. E. W. Bauer, Angular and linear momentum of excited ferromagnets, *Phys. Rev. B* **88**, 144413 (2013).
- [21] X.-G. Wang, G.-H. Guo, G.-F. Zhang, Y.-Z. Nie, and Q.-L. Xia, Spin-wave resonance reflection and spin-wave induced domain wall displacement, *J. Appl. Phys.* **113**, 213904 (2013).
- [22] X.-G. Wang, G.-H. Guo, G.-F. Zhang, Y.-Z. Nie, and Q.-L. Xia, An analytical approach to the interaction of a propagating spin wave and a Bloch wall, *Appl. Phys. Lett.* **102**, 132401 (2013).
- [23] X.-G. Wang, G.-H. Guo, Y.-Z. Nie, G.-F. Zhang, and Z.-X. Li, Domain wall motion induced by the magnonic spin current, *Phys. Rev. B* **86**, 054445 (2012).
- [24] J. Xia, Y. Huang, X. Zhang, W. Kang, C. Zheng, X. Liu, W. Zhao, and Y. Zhou, A microwave field-driven transistor-like skyrmionic device with the microwave current-assisted skyrmion creation, *J. Appl. Phys.* **122**, 153901 (2017).
- [25] M. J. Donahue and D. G. Porter, OOMMF User's Guide, Version 1.0, Tech. Rep. NISTIR 6376 (National Institute of Standards and Technology, Gaithersburg, MD, 1999).
- [26] S. Rohart and A. Thiaville, Skyrmion confinement in ultrathin film nanostructures in the presence of Dzyaloshinskii-Moriya interaction, *Phys. Rev. B* **88**, 184422 (2013).
- [27] S. Li, J. Xia, X. Zhang, M. Ezawa, W. Kang, X. Liu, Y. Zhou, and W. Zhao, Dynamics of a magnetic skyrmionium driven by spin waves, *Appl. Phys. Lett.* **112**, 142404 (2018).
- [28] A. A. Thiele, Steady-State Motion of Magnetic Domains, *Phys. Rev. Lett.* **30**, 230 (1973).
- [29] R. Tomasello, E. Martinez, R. Zivieri, L. Torres, M. Carpentieri, and G. Finocchio, A strategy for the design of skyrmion race-track memories, *Sci. Rep.* **4**, 6784 (2014).
- [30] O. A. Tretiakov, D. Clarke, G.-W. Chern, Y. B. Bazaliy, and O. Tchernyshyov, Dynamics of Domain Walls in Magnetic Nanostrips, *Phys. Rev. Lett.* **100**, 127204 (2008).
- [31] P. Upadhyaya, G. Yu, P. K. Amiri, and K. L. Wang, Electric-field guiding of magnetic skyrmions, *Phys. Rev. B* **92**, 134411 (2015).
- [32] C. Navau, N. Del-Valle, and A. Sanchez, Interaction of isolated skyrmions with point and linear defects, *J. Magn. Magn. Mater.* **465**, 709 (2018).
- [33] C. Navau, N. Del-Valle, and A. Sanchez, Analytical trajectories of skyrmions in confined geometries: Skyrmionic racetracks and nano-oscillators, *Phys. Rev. B* **94**, 184104 (2016).
- [34] S. Schroeter and M. Garst, Scattering of high-energy magnons off a magnetic skyrmion, *Low Temp. Phys.* **41**, 817 (2015).
- [35] C. Schütte and M. Garst, Magnon-skyrmion scattering in chiral magnets, *Phys. Rev. B* **90**, 094423 (2014).
- [36] W. Wang, M. Albert, M. Beg, M.-A. Bisotti, D. Chernyshenko, D. Cortés-Ortuño, I. Hawke, and H. Fangohr, Magnon-Driven Domain-Wall Motion with the Dzyaloshinskii-Moriya Interaction, *Phys. Rev. Lett.* **114**, 087203 (2015).
- [37] J. Iwasaki, W. Koshibae, and N. Nagaosa, Colossal spin transfer torque effect on skyrmion along the edge, *Nano Lett.* **14**, 4432 (2014).
- [38] X. S. Wang, H. Y. Yuan, and X. R. Wang, A theory on skyrmion size, *Commun. Phys.* **1**, 31 (2018).
- [39] H.-B. Braun, Fluctuations and instabilities of ferromagnetic domain-wall pairs in an external magnetic field, *Phys. Rev. B* **50**, 16485 (1994).
- [40] A. Kosevich, B. Ivanov, and A. Kovalev, Magnetic solitons, *Phys. Rep.* **194**, 117 (1990).
- [41] G. Venkat, D. Kumar, M. Franchin, O. Dmytriiev, M. Mruczkiewicz, H. Fangohr, A. Barman, M. Krawczyk, and A. Prabhakar, Proposal for a standard micromagnetic problem: Spin wave dispersion in a magnonic waveguide, *IEEE Trans. Magn.* **49**, 524 (2013).
- [42] J. Zang, M. Mostovoy, J. H. Han, and N. Nagaosa, Dynamics of Skyrmion Crystals in Metallic thin Films, *Phys. Rev. Lett.* **107**, 136804 (2011).
- [43] J. Iwasaki, M. Mochizuki, and N. Nagaosa, Current-induced skyrmion dynamics in constricted geometries, *Nat. Nanotechnol.* **8**, 742 (2013).
- [44] Y.-G. Choi and G.-M. Choi, Investigation of stiffness and damping constant of spin waves in a soft magnet $\text{Co}_{100-x}\text{B}_x$ alloy, *Appl. Phys. Lett.* **121**, 012404 (2022).
- [45] A. V. Chumak, A. A. Serga, and B. Hillebrands, Magnonic crystals for data processing, *J. Phys. D: Appl. Phys.* **50**, 244001 (2017).
- [46] X. Liu, W. Zhang, M. J. Carter, and G. Xiao, Ferromagnetic resonance and damping properties of CoFeB thin films as free layers in MgO-based magnetic tunnel junctions, *J. Appl. Phys.* **110**, 033910 (2011).
- [47] A. Conca, E. T. Papaioannou, S. Klingler, J. Greser, T. Sebastian, B. Leven, J. Lösch, and B. Hillebrands, Annealing influence on the gilbert damping parameter and the exchange constant of CoFeB thin films, *Appl. Phys. Lett.* **104**, 182407 (2014).
- [48] <https://doi.org/10.5518/1363>.